

*School of Natural Sciences and Mathematics*

***Observational Evidence of the Drift-Mirror  
Plasma Instability in Earth's Inner Magnetosphere***

**UT Dallas Author(s):**

Zhiyang Xia  
Lunjin Chen

**Rights:**

CC BY 4.0 (Attribution)  
©2019 The Authors

**Citation:**

Soto-Chavez, A. R., L. J. Lanzerotti, J. W. Manweiler, A. Gerrard, et al.  
2019. "Observational evidence of the drift-mirror plasma instability in  
Earth's inner magnetosphere." *Physics of Plasmas* 26(4): art. 042110, doi:  
10.1063/1.5083629

*This document is being made freely available by the Eugene McDermott Library  
of the University of Texas at Dallas with permission of the copyright owner. All  
rights are reserved under United States copyright law unless specified otherwise.*

# Observational evidence of the drift-mirror plasma instability in Earth's inner magnetosphere

Cite as: Phys. Plasmas **26**, 042110 (2019); <https://doi.org/10.1063/1.5083629>

Submitted: 29 November 2018 . Accepted: 07 March 2019 . Published Online: 10 April 2019

A. R. Soto-Chavez , L. J. Lanzerotti , J. W. Manweiler , A. Gerrard , R. Cohen, Z. Xia, L. Chen, and H. Kim 



View Online



Export Citation



CrossMark

## ARTICLES YOU MAY BE INTERESTED IN

[Multi-region relaxed magnetohydrodynamic stability of a current sheet](#)

Physics of Plasmas **26**, 030702 (2019); <https://doi.org/10.1063/1.5091765>

[Fast magnetic reconnection and the ideal evolution of a magnetic field](#)

Physics of Plasmas **26**, 042104 (2019); <https://doi.org/10.1063/1.5081828>

[On the generalized formulation of Debye shielding in plasmas](#)

Physics of Plasmas **26**, 050701 (2019); <https://doi.org/10.1063/1.5091949>

AIP Conference Proceedings  
**FLASH WINTER SALE!**

**50% OFF** ALL PRINT PROCEEDINGS

ENTER CODE 50DEC19 AT CHECKOUT



# Observational evidence of the drift-mirror plasma instability in Earth's inner magnetosphere

Cite as: Phys. Plasmas **26**, 042110 (2019); doi: [10.1063/1.5083629](https://doi.org/10.1063/1.5083629)

Submitted: 29 November 2018 · Accepted: 7 March 2019 ·

Published Online: 10 April 2019



View Online



Export Citation



CrossMark

A. R. Soto-Chavez,<sup>1</sup>  L. J. Lanzerotti,<sup>1</sup>  J. W. Manweiler,<sup>2</sup>  A. Gerrard,<sup>1</sup>  R. Cohen,<sup>1</sup> Z. Xia,<sup>3</sup> L. Chen,<sup>3</sup> and H. Kim<sup>1</sup> 

## AFFILIATIONS

<sup>1</sup>Center for Solar-Terrestrial Research, New Jersey Institute of Technology, Newark, New Jersey 07102, USA

<sup>2</sup>Fundamental Technologies, LLC, Lawrence, Kansas 66046, USA

<sup>3</sup>Physics Department, University of Texas at Dallas, Dallas, Texas 75080, USA

## ABSTRACT

We report on evidence for the generation of an ultra-low frequency plasma wave by the drift-mirror plasma instability in the dynamic plasma environment of Earth's inner magnetosphere. The plasma measurements are obtained from the Radiation Belt Storm Probes Ion Composition Experiment onboard NASA's Van Allen Probes Satellites. We show that the measured wave-particle interactions are driven by the drift-mirror instability. Theoretical analysis of the data demonstrates that the drift-mirror mode plasma instability condition is well satisfied. We also demonstrate, for the first time, that the measured wave growth rate agrees well with the predicted linear theory growth rate. Hence, the *in-situ* space plasma observations and theoretical analysis demonstrate that local generation of ultra-low frequency and high amplitude plasma waves can occur in the high beta plasma conditions of Earth's inner magnetosphere.

© 2019 Author(s). All article content, except where otherwise noted, is licensed under a Creative Commons Attribution (CC BY) license (<http://creativecommons.org/licenses/by/4.0/>). <https://doi.org/10.1063/1.5083629>

## I. INTRODUCTION

The drift-mirror (DM) plasma instability<sup>1</sup> and its significance for fundamental plasma physics have been discussed for several decades. The significance of the DM is that while it is recognized as fundamental in plasma physics, it can only be realized and studied in space and astrophysical contexts. For example, laboratory plasma confinement devices are not designed for high beta plasma conditions that are required for the onset of the DM instability.<sup>1,2</sup> The DM is a low frequency plasma mode (below the ion gyro-frequency) and its excitation, in its simplest form, requires that the plasma pressure times the plasma temperature anisotropy be larger than the magnetic field pressure. Mirror modes, on the other hand, are a special case of a DM plasma wave. That is, mirror modes are pure growing compressional plasma modes that are non-oscillatory (zero real frequency) but whose instability condition is the same as that of the DM modes. The difference between the two is that a DM mode has a real frequency part equal to the plasma drift frequency.<sup>1,3</sup> This is because by including inhomogeneity effects in density and magnetic field, Hasegawa<sup>1</sup> showed that the instability picks up a real frequency part (without changing the imaginary part of the mode) via coupling to drift waves. And so, both modes have the same instability threshold and growth rate.

A necessary (but not sufficient) condition for the DM instability is that the plasma beta parameter  $\beta_{\perp}$  (a ratio of plasma pressure to

magnetic field pressure) in the perpendicular direction be larger than one.<sup>4</sup> Theoretical understanding of the DM mode excitation in the linear regime is well understood, i.e., DM instability arises due to temperature anisotropy of the plasma. However, unlike the pure mirror instability the DM instability depends critically on the wave-particle resonant interactions (see, e.g., Ref. 3, and references therein). The nonlinear evolution, however, remains an active area of research (see, e.g., Ref. 5). Analysis and further developments to the theory of the DM plasma instability are, however, outside the scope of this study.

Ultra-low frequency (ULF) waves in Earth's magnetosphere can be generated externally or internally. Internally generated ULF waves are often associated with plasma instabilities in Earth's Ring Current.<sup>6</sup> Among the plasma instabilities associated with the generation of ULF waves is the DM plasma instability. The importance of ULF modes in Earth's magnetosphere cannot be overstated since lower frequency modes are much more powerful than high frequency modes in space plasmas.<sup>7,8</sup> It has also been shown that large amplitude low frequency modes can diffuse particles efficiently (see, e.g., Refs. 6 and 9).

There is reported evidence for the DM mode (i.e., ULF wave generated by the DM plasma instability) in the Earth's magnetosphere at very high altitudes  $L \equiv r_{eq}/R_E > 8$  where  $L$  is the  $L$ -shell parameter and  $r_{eq}$  and  $R_E$  are the equatorial radial distance from Earth and the Earth's radius ( $R_E \approx 6,371$  km), respectively. For example, low

frequency waves attributed to DM modes have been reported in Earth's dayside magnetosheath (see, e.g., Refs. 10–12), at bow shock crossings,<sup>13</sup> in the dawn side plasma sheet,<sup>14–16</sup> magnetospheric flanks,<sup>17</sup> However, in all the aforementioned studies, it has never been possible to simultaneously measure the wave growth rate (predicted by the DM linear theory) and to satisfy the condition of the DM plasma instability successfully.

In Earth's inner magnetosphere ( $L < 6$ ), where plasma conditions can be highly variable, the generation of the DM mode has not been conclusively demonstrated. The first known report of the likely occurrence of the DM mode in space plasmas (in the inner magnetosphere in fact) was reported by Lanzerotti, Hasegawa, and MacLennan;<sup>18</sup> however, the instability criterion was not satisfied and the growth rate was not quantified. Later, studies on the generation of ultra low frequency waves by the DM instability at geostationary orbits were carried out;<sup>19,20</sup> however, the DM instability condition was not satisfied. Because the DM instability threshold is difficult to satisfy in Earth's inner magnetosphere, other modes such as the Drift-Compressional Modes (DCM) have been proposed to explain some satellite observations.<sup>21,22</sup>

Recently, Xia *et al.*<sup>23</sup> reported the modulation of magnetosphere chorus waves (for more on chorus see, e.g., Soto-Chavez *et al.*,<sup>24</sup> and references therein) by a strong field line resonance mode which shows signatures of coupling with a DM mode. The signatures of the ULF wave were qualitatively attributed to a DM mode, but no quantitative evidence for this attribution was provided.

In this study, we report conclusive evidence of the generation of a DM mode in the high beta plasma environment of Earth's inner magnetosphere using data from NASA's Van Allen Probes. By conclusive evidence, we mean that not only the instability criterion is found to be satisfied in the present study but also the wave growth rate of the DM theory agrees well with that obtained from the observation. As mentioned above, past studies have often observed wave-particle characteristics generally consistent with the DM instability, such as anti-correlations between wave and plasma pressure, but those satellite observations (in Earth's inner magnetosphere) have generally failed to satisfy the instability condition and the wave growth rate has never been directly measured and corroborated.

Our observations and analysis provide important insights into the plasma conditions for the development of ULF waves by DM instability and confirm predictions of fundamental plasma physics for the generation of the DM instability. The conditions under which the mode is established in the deep inner magnetosphere have significant implications in ring current dynamics, because ULF modes can be involved with particle energization and diffusion.<sup>1,6,9</sup> Importantly, these results provide fundamental information on the physics of high beta plasmas that can only be obtained with modern *in-situ* measurements.

The present study is organized as follows. In Sec. II, we list the instrumentation and data used. In Sec. III, we present the observations and wave-particle characteristics indicative of the DM instability. In Sec. IV, we evaluate the DM instability condition and growth rate from the data and compare it to the theory predictions. We conclude the study with the discussions, Sec. V, and conclusions Sec. VI.

## II. INSTRUMENTATION AND DATA

NASA's two Van Allen Probes satellites were launched on 30 August 2012<sup>25</sup> with the objective of quantitatively understanding the radiation environment of the Earth's magnetosphere, of which the ring

current is an important component. The measurements used in this study were obtained from the time-of-flight by pulse height low-energy and high-time resolution (TOF  $\times$  PHLEHT) proton observations ( $\approx 8$ –50 keV) and the time-of-flight by energy (TOF  $\times$  E) proton observations ( $\approx 45$ –600 keV) of the Radiation Belt Storm Probes Ion Composition Experiment (RBSPICE-B) instrument onboard Van Allen Probe B. The RBSPICE instrument provides excellent energy and angular resolution coverage of multi-heavy ion species, i.e., H ions, He ions, and O ions as well as electrons (Mitchell *et al.*,<sup>26</sup> Soto-Chavez *et al.*,<sup>27</sup> and references therein). Specifically, we used Level 3 Pitch Angle and Pressure (PAP) data from RBSPICE-B instrument which is sampled at spacecraft spin resolution  $\sim 11$  s. We also use data from the EMFISIS-B wave instrument magnetometer at 4 s resolution<sup>28</sup> onboard the Van Allen Probe B which provide the magnetic field measurements. Because the data, from the different instruments, are sampled at different time resolutions, we resampled the data to the common time resolution of the RBSPICE data when needed, e.g., when calculating the cross-phase coherence analysis between the magnetic field wave and energetic particle observations. Also, low-pass and band-pass filtering is used to detrend the data when needed.

## III. MEASUREMENTS AND WAVE-PARTICLE SIGNATURES OF THE DM INSTABILITY

Recently, a statistical survey of high-beta plasma events (covering a full orbit precession of NASA's Van Allen Probes: 9 March 2013–31 December 2014) in Earth's inner magnetosphere was carried out.<sup>29</sup> One of these high beta  $\beta$  ( $\beta = P_{\text{plasma}}/P_B$ , see Sec. V for pressure definitions) events is shown in Fig. 1. The top panel shows that, on July 6, 2013, during the second orbit of Van Allen Probe B, the  $\beta$  value was largely  $> 1$  throughout the orbit. The bottom panel shows the energy spectrogram for the H ions showing injections of energetic ions at times during the orbit. Note that when the ions are injected from the tail into the inner magnetosphere, they are usually heated by two processes: Fermi and betatron acceleration.<sup>30</sup> Fermi acceleration is caused by conservation of the second adiabatic invariant and betatron acceleration is due to conservation of the first adiabatic invariant. This occurs when the particles are transported (convectively) into the inner magnetosphere experiencing higher magnetic fields and therefore conservation of the aforementioned invariants forces them to gain energy. The end result of these processes is that the ions will develop higher perpendicular energies than the parallel. The time scales for the ion transport to the magnetosphere depend mostly on  $L$ -value and energy. In the inner magnetosphere ( $L < 6$ ), the timescales are on the order of the ion drift period<sup>31</sup>  $\langle t_D \rangle \propto E^{-1}L^{-1}$ , which for the energies ( $E$ ) here considered is on the order of 1–10 h. For comparison, the ion bounce drift period for the energies herein considered is  $t_b \propto L/E^{1/2} \approx 20$ –60 s.

Figures 2 and 3 show an overview of the magnetic field and plasma parameters between  $\approx 13:00$  and 15:00 UTC. (i.e., within the second orbit as shown in Fig. 1.) The top panel in Fig. 2 shows the total magnetic field in GSM coordinates; therein, a wave is seen with maximum oscillations (the peak to peak amplitude oscillation is  $\approx 20$  nT) at  $\approx 13:50$ –14:20 UTC, though the mode was actually generated at  $\approx 13:28$ –29 UTC (see Sec. IV). The wave period is  $\approx 150$  s or 6.6 mHz, i.e., a ULF wave (Pc 5 freq. band). The lower left three panels in Fig. 2 show the GSM X, Y, Z components of the magnetic field. The lower right three panels show a zoom in ( $\approx 13:20$ –14:40 UTC) region of the magnetic field in Mean-Field-Aligned (MFA) coordinates:  $B_{\parallel}$ ,  $B_{\phi}$ ,  $B_r$ .

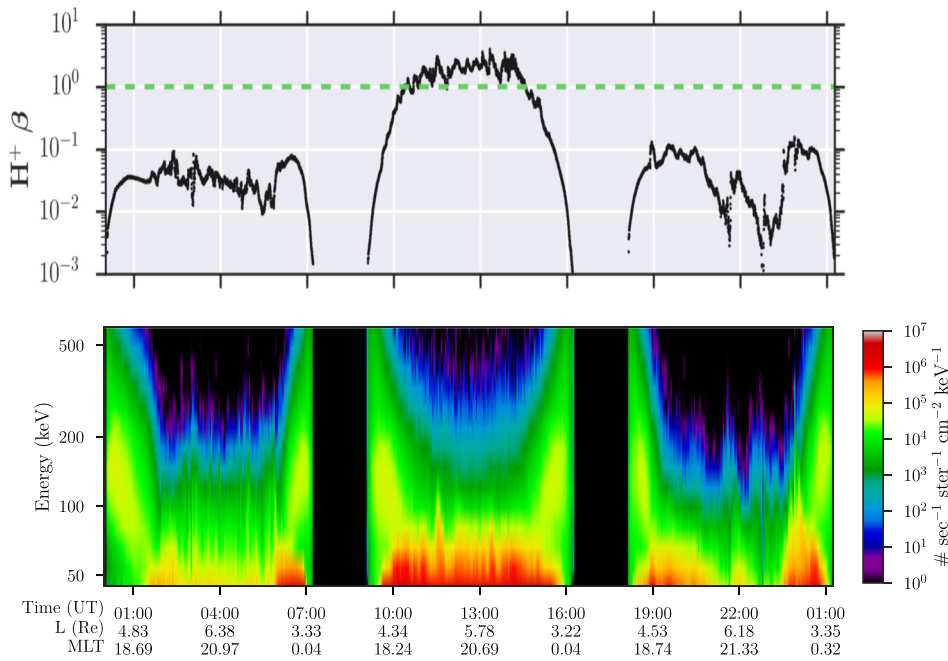


FIG. 1. Top: plasma beta value of H ions (TOF  $\times$  E only). Bottom: energy spectrogram for H ions only (TOF  $\times$  E). The horizontal green line indicates  $\beta = 1$ . Note that during much of the second orbit ( $\sim 10$ – $16$  UTC)  $\beta > 1$ . MLT = magnetic local time.

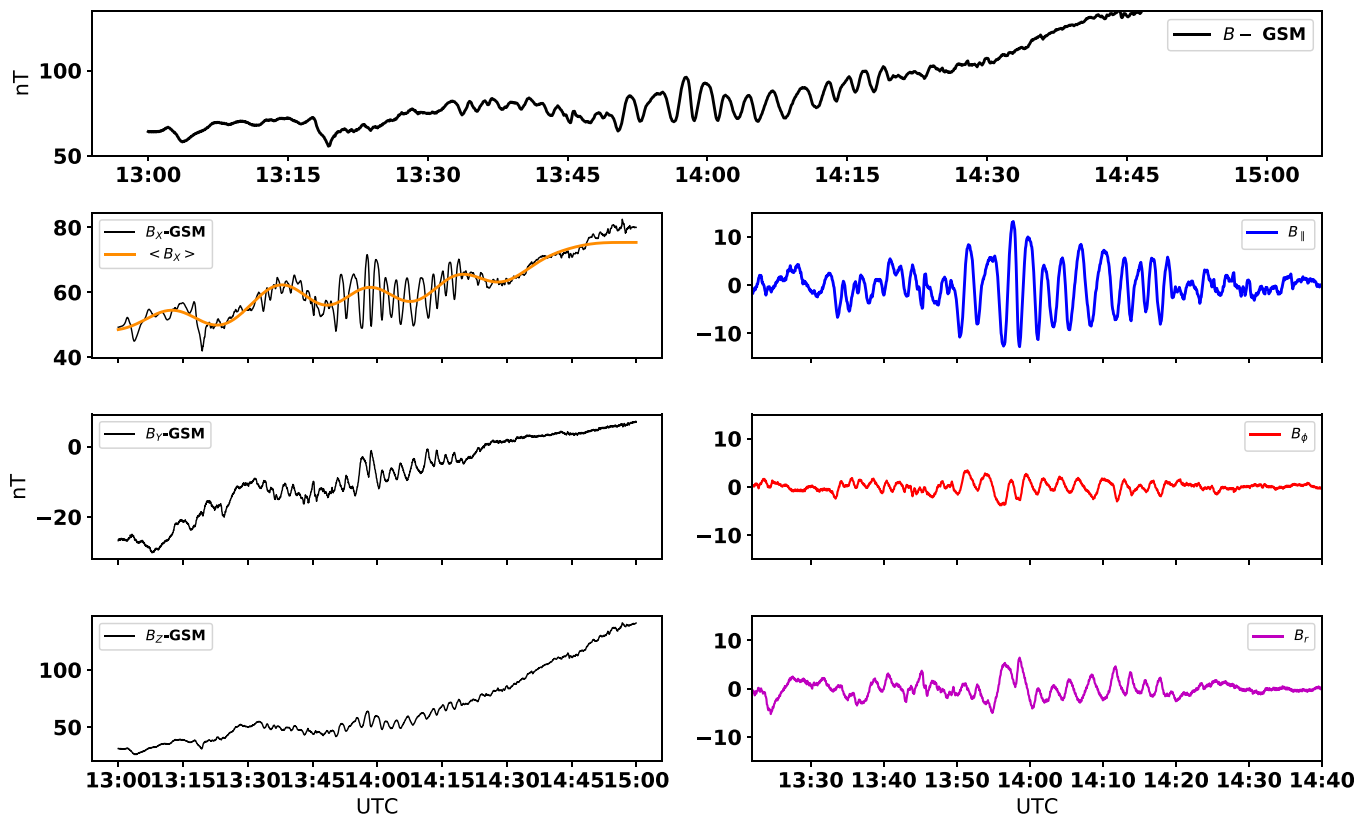
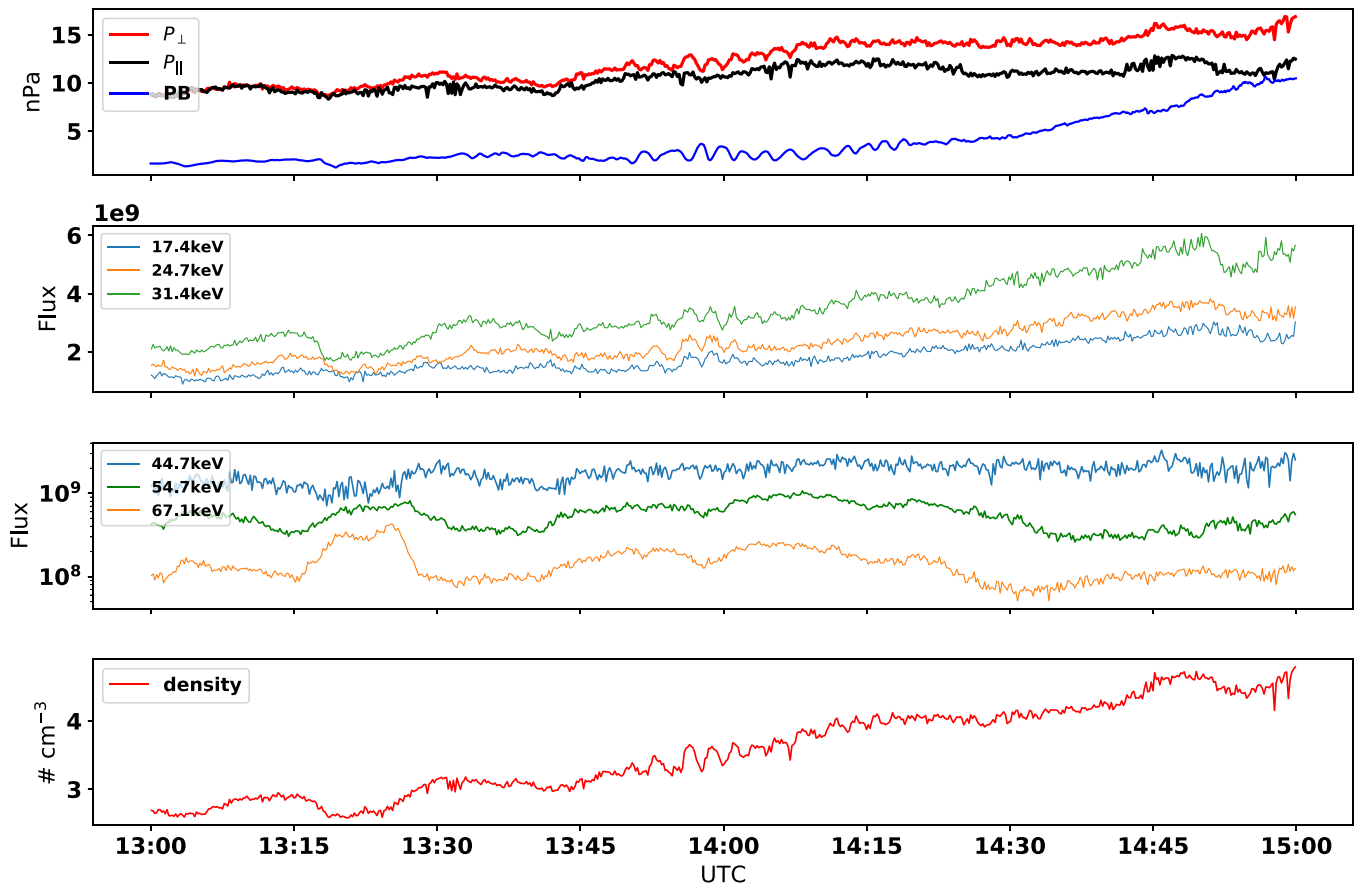


FIG. 2. Top: (unfiltered) total magnetic field (B) in GSM coordinates at 4 s resolution from EMFISIS-B. Bottom left three panels: the GSM X, Y, Z magnetic field components. The orange-color trace represents (one component) the mean average magnetic field, which is calculated as explained in the text. Right panels: A zoom in region of the magnetic field in MFA coordinates.



**FIG. 3.** Top, partial plasma pressures:  $P_{\perp}$  and  $P_{\parallel}$ , red and black lines (respectively) and magnetic field pressure (blue line). Middle panels: H-ion fluxes ( $\text{counts} \cdot \text{s}^{-1} \cdot \text{ster}^{-1} \cdot \text{cm}^{-2} \cdot \text{MeV}^{-1}$ ) at a  $90^{\circ}$  pitch angle (PA). Bottom panel: H-ion partial density ( $\text{particles} \cdot \text{cm}^{-3}$ ) calculated from the H-ion fluxes ( $E \approx 17\text{--}67$  keV). Note that only the third panel from the top is shown on a logarithmic scale.

It is evident that the  $B_{\parallel}$  is the largest component, and therefore, the magnetic wave is mostly compressional, consistent with  $\mathbf{a}_{\perp}$  DM mode.<sup>1,3,6</sup>  $B_{\parallel}$  is calculated by  $B_{\parallel} = \vec{e}_{\parallel} \cdot \vec{B} - \langle B \rangle$ , where  $\vec{e}_{\parallel} \equiv \langle \vec{B} \rangle / \langle B \rangle$  is a parallel unit vector along the average (smooth) magnetic field  $\langle B \rangle$ . The average magnetic field is created by low-pass filtering the B field data with a cut-off frequency  $f_c = 1$  mHz, as indicated by the orange-color trace in Fig. 2. The other components are then chosen to be  $\vec{e}_{\phi} \sim \vec{r} \times \vec{e}_{\parallel}$  ( $B_{\phi} = \vec{e}_{\phi} \cdot \vec{B}$ ), where  $\vec{r}$  is a radius unit vector of the satellite position and  $\vec{e}_r \sim \vec{e}_{\parallel} \times \vec{e}_{\phi}$  ( $B_r = \vec{e}_r \cdot \vec{B}$ ) completes the right-handed orthogonal system (for more on MFA coordinates see, e.g., Refs. 32 and 33).

Figure 3 shows an overview of the plasma parameters and fluxes during the same time interval as in Fig. 2. The top panel shows the perpendicular  $P_{\perp}$  and parallel  $P_{\parallel}$  partial plasma pressures (with respect to the background magnetic field, see Sec. V for pressure definitions) and the magnetic field pressure  $P_B = B^2/2\mu_0$ . Here,  $B$  is the magnetic field magnitude and  $\mu_0$  is the vacuum permeability. It can be seen (especially for  $P_{\perp}$ ) that during interval  $\approx 13:50\text{--}14:10$  UTC the pressures oscillate in anti-phase with the  $P_B$  oscillations. The next panel shows the H-ion fluxes ( $\approx 17\text{--}31$  keV energy range); here, the

flux oscillations (which are in anti-phase with respect to the  $P_B$ ) are clearly seen at about 13:50 UTC. The following panel shows the fluxes for the energies  $\approx 45\text{--}67$  keV, and finally the last panel shows the density of H-ions (energy range 17–67 keV). Note that Van Allen Probe B was right at the magnetic equator, see Fig. 4. However, as reported in Xia *et al.*,<sup>23</sup> the Van Allen Probe A was trailing B by  $>4$  h. and missed the wave event completely. The reason is that the actual spacecraft separation distance between the A–B probes during 13:28–14:20 UTC time interval varies from  $5.85R_E$  to  $4.6R_E$ , respectively, which equates to a separation of  $\sim 6$  h MLT. This distance, as we shall see in Sec. IV, is much larger than the perpendicular wavelength of the ULF wave.

In Fig. 5, we zoom in further to 13:50–14:10 UTC where the anti-correlations between the parallel component of the wave in the magnetic field  $B_{\parallel}$ , the plasma density (45–600 keV ions), and the H-ion fluxes at  $E = 55$  keV can be seen.

The anti-phase correlations (the Pearson correlation coefficient between wave and density, at the interval shown in Fig. 5, is  $-0.65$ ), which lasted for about 20 min., between wave and density and fluxes are potentially indicative of wave generation by the DM instability,<sup>1,18</sup>

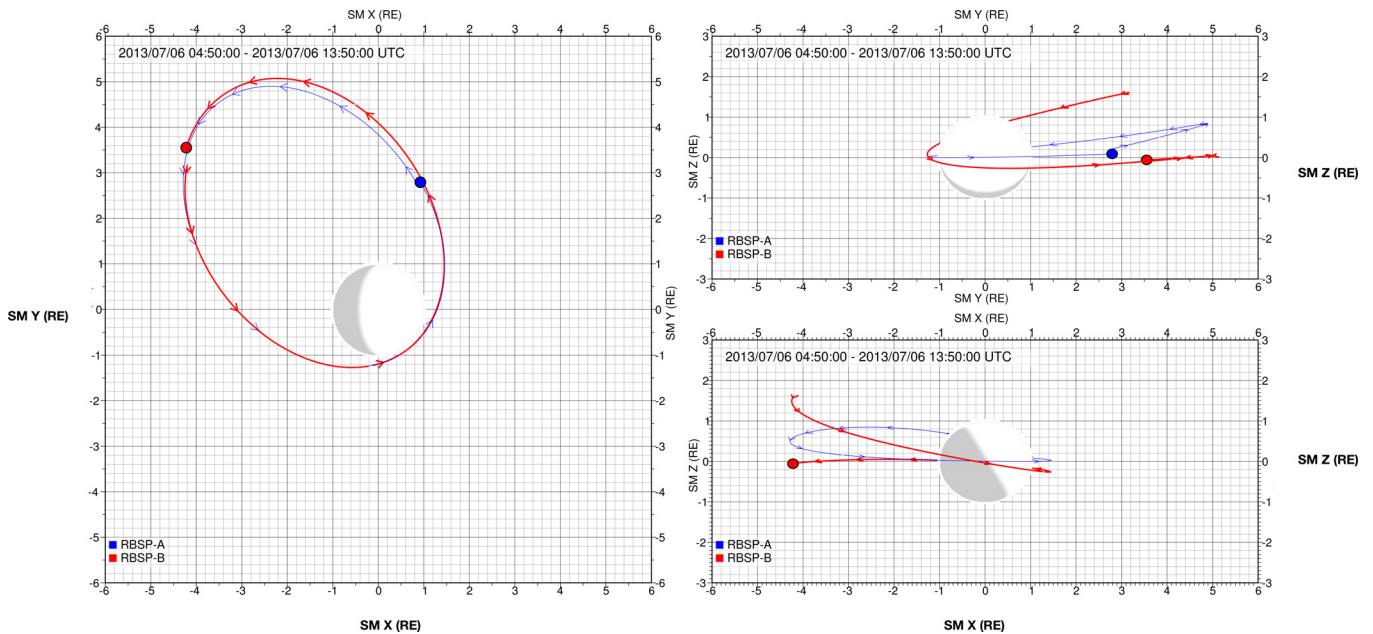


FIG. 4. Van Allen Probe B (red dot) and A (blue dot) spacecraft positions at 13:50 UTC. The tick mark (arrow) interval = 1 h. The spacecraft A was more than 4 h way from B missing the wave event.

because according to theory  $\delta n = (1 - P_{\perp}/P_{\parallel})B_{\parallel}$ . Here,  $\delta n$  and  $B_{\parallel}$  represent the variations of density and parallel magnetic field component. Hence, when  $P_{\perp} > P_{\parallel}$ , the density and magnetic field variations are in anti-phase, as seen in this event. In Fig. 6, the wave and ion fluxes at different energies are shown. The correlation coefficients between wave and fluxes are  $-0.79$ ,  $-0.85$ , and  $-0.74$ , for the 45, 55, and 67 keV energy channels, respectively.

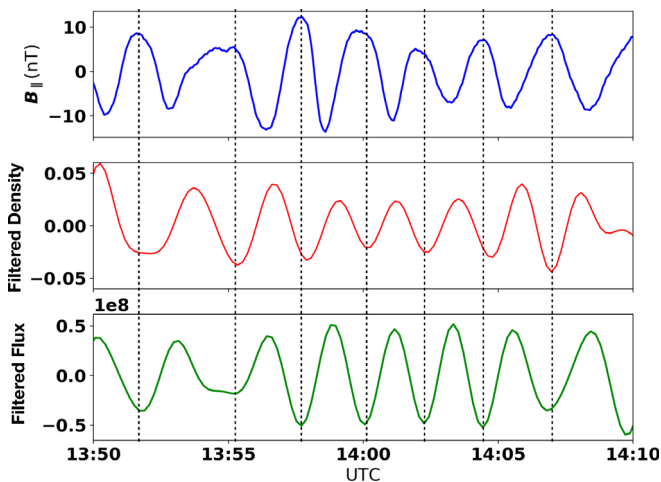


FIG. 5. Top:  $B_{\parallel}$ -component of the magnetic field at 4 s resolution from EMFISIS-B. Middle: Band-pass filtered (as described in text) H-ion (45–600 keV) partial density (particles  $\cdot$  cm $^{-3}$ ), from RBSPICE-B. Bottom: Band-pass filtered 90° PA H ion fluxes, from RBSPICE-B. The fluxes (counts  $\cdot$  s $^{-1}$   $\cdot$  ster $^{-1}$   $\cdot$  cm $^{-2}$   $\cdot$  MeV $^{-1}$ ) shown are from the RBSPICE-B 55 keV energy channel only.

Note that in Figs. 5 and 6, the density and fluxes (for  $E \geq 45$  keV only) have been band-pass filtered (with a 3 dB cut-off at frequencies 4 mHz and 10 mHz; therefore, the positive and negative flux values are shown in Figs. 5 and 6) unlike the case for the fluxes with  $E \approx 17$ –31 keV shown in Fig. 6. The filtered flux data in Figs. 5 and 6 are presented to show further evidence that there are indeed anti-correlations between the wave, density, and the high energy fluxes at  $\approx 45$ , 55, and 67 keV, which are not obvious in Fig. 3. The same can be said for the H-ion density, which in Fig. 5 is flux-integrated in the energy range  $\approx 45$ –600 keV.

Finally, in Fig. 7, we present, for completeness, a cross-correlation wavelet analysis<sup>34</sup> between the wave  $B_{\parallel}$  and the  $\approx 45$  keV H ion fluxes, for a longer time interval, 13:40–14:40 (1 h), than previously shown in Figs. 5 and 6. We can see that the wavelet analysis technique of cross-correlation picks a high-coherence region between fluxes and wave at  $\approx 150$  s. period from 13:50–14:10, just as the above time filtered analysis indicates. The arrows in Fig. 7 point towards the left indicating an almost 180° out-of-phase difference, corroborating the above analysis. Of course, the wavelet analysis gives more information such as other coherence regions but these other coherent regions are at different frequencies of interest and much smaller.

Therefore, as shown above, all the wave-particle interactions indicate that the DM plasma instability is at play. To confirm this, we calculate in Sec. IV the DM instability condition and determine the wave growth rate.

#### IV. WAVE GENERATION MECHANISM: DM INSTABILITY CONDITION AND WAVE GROWTH

The local linear theory instability condition for the DM wave mode generation in the low frequency and long wave period limits,

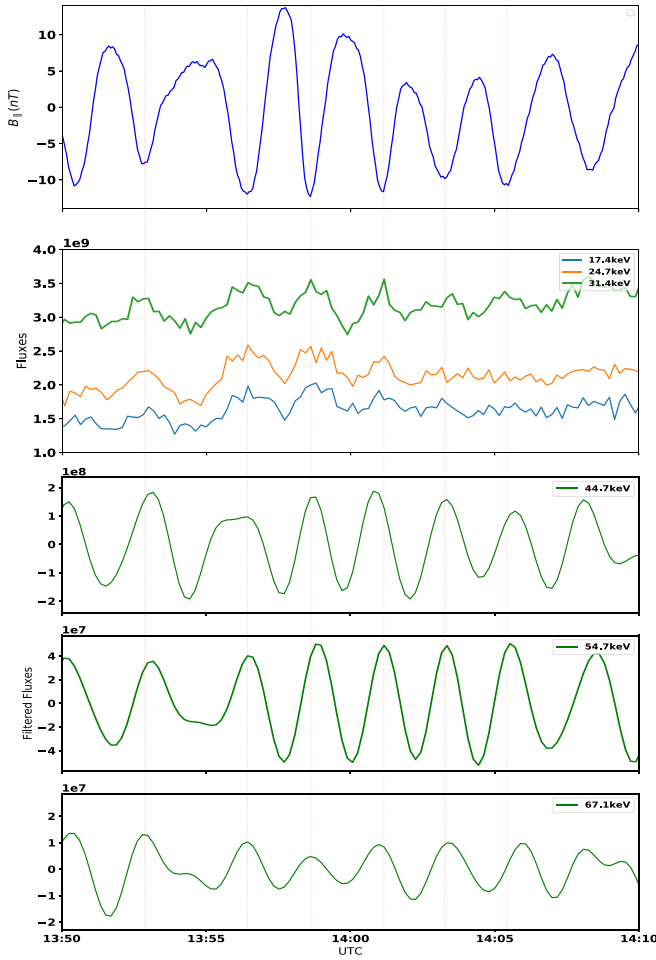


**FIG. 6.** Top panel:  $B_{\parallel}$ -component of the magnetic field at 4 s resolution from EMFISIS-B. Second (from top): unfiltered H-ion fluxes at  $90^{\circ}$  PA, from RBSP/ICE-B. The differential fluxes (counts  $\cdot$  s $^{-1}$   $\cdot$  ster $^{-1}$   $\cdot$  cm $^{-2}$   $\cdot$  keV $^{-1}$ ) shown are from the  $\approx 17$ – $31$  keV TOF  $\times$  PH energy channels. Third to fifth panels: Band-pass filtered (as described in text)  $90^{\circ}$  PA H-ion fluxes (counts  $\cdot$  s $^{-1}$   $\cdot$  ster $^{-1}$   $\cdot$  cm $^{-2}$   $\cdot$  MeV $^{-1}$ ). From  $\approx 45$ – $67$  keV TOF  $\times$  E energy channels.

i.e.,  $\omega \ll \Omega_i$ , and  $k_{\perp} v_{\perp} / \Omega_i \ll 1$ ,  $k_{\parallel} v_{\parallel} / \Omega_i \ll 1$  and  $k_{\parallel} \ll k_{\perp}$ , with a particle bi-Maxwellian distribution for the ions (cold electrons) is

$$P_{\perp}(P_{\perp}/P_{\parallel} - 1) > P_B \quad (1)$$

or in terms of beta $^1$  ( $P_{\perp}/P_{\parallel} - 1$ )  $>$   $\beta_{\perp}^{-1}$ . Here,  $\beta_{\perp} = P_{\perp}/P_B$ ,  $\omega$  and  $\Omega_i$  are the wave and ion angular frequencies, respectively,  $k$  is the wave number, and  $v_{\perp, \parallel}$  are the ion perpendicular and parallel thermal speeds. The perpendicular and parallel directions are with respect to the background magnetic field. The extension to multiple ion species  $s$  (cold electrons) is trivial, $^1$  and the instability condition simply becomes  $\sum_s \beta_{s\perp}(P_{s\perp}/P_{s\parallel} - 1) > 1$ . We scanned the data before the time 13:50 UTC (i.e., before the onset of the strong wave-particle anti-phase correlations) to test for the DM instability condition. We found an interval in time (during the long interval of  $\beta > 1$  conditions) where the DM instability condition was satisfied, at  $\approx 13:28$ – $29$  UTC. With

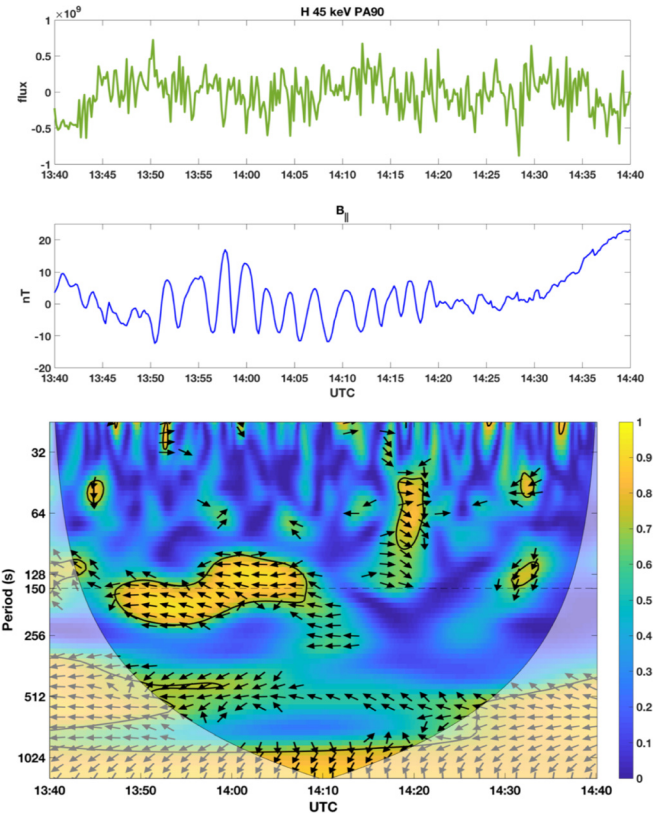


**FIG. 7.** Top panel:  $90^{\circ}$  PA, 45 keV H-ion fluxes (counts  $\cdot$  s $^{-1}$   $\cdot$  ster $^{-1}$   $\cdot$  cm $^{-2}$   $\cdot$  MeV $^{-1}$ ). Middle:  $B_{\parallel}$ -component of the magnetic field, same as in Figs. 5 and 6. Bottom: cross-phase coherence wavelet analysis between the two time series above. The arrows indicate the phase-angle between the time series, the arrow key is as follows: pointing to the right  $0^{\circ}$ , up  $90^{\circ}$ , left  $180^{\circ}$ , down  $270^{\circ}$ . The y-axis in the bottom panel is on a  $\log_2$  scale.

six energy channels in total, i.e., three energy channels (17, 24, 31 keV) from TOF  $\times$  PHLEHT proton rate data and three energy channels (45, 55, 67 keV) from TOF  $\times$  E proton rate data, we find that  $P_{\perp}(P_{\perp}/P_{\parallel} - 1) = 2.58$  nPa and  $P_B = 2.21$  nPa.

We note that in the above limits (low frequency and long wave periods), the *maximum* wave growth $^{35}$  is given by

$$\gamma_m = \left[ \frac{\Omega_s}{4\sqrt{3\pi}} \right] \left[ \Gamma_s^2 / (\beta_{s\perp} A_s^{3/2} \Pi_s^{1/2}) \right], \quad (2)$$

where  $\Gamma_s = \beta_{s\perp}(P_{s\perp}/P_{s\parallel} - 1) - 1$ ,  $A_s = P_{s\perp}/P_{s\parallel}$  is the plasma anisotropy and  $\Pi_s = 1 + (\beta_{s\perp} - \beta_{s\parallel})/2$ . Note that the maximum growth rate  $\gamma_m \propto \Gamma_s^2$ , where  $\Gamma_s > 1$ . The maximum wave numbers are  $k_{m\perp} = (1/r_{gs})\sqrt{\Gamma_s/6}$  and  $k_{m\parallel} = \Gamma_s / (2\sqrt{6}r_{gs}\Pi_s^{1/2})$ . Here,  $r_{gs}$  is the species Larmor radius. Now, with the measured plasma data for the event, shown in Table I, we obtain an analytical maximum growth rate  $\gamma_m = 0.0018$  s $^{-1}$  and a perpendicular wavelength  $\lambda_{m\perp} = 7772$  km or  $1.22R_E$ , which approximates to an azimuthal wave number  $m \equiv 2\pi r / \lambda_{\perp} \approx 28$  ( $r = 5.6R_E$ ). The maximum parallel wavelength is  $\lambda_{\parallel} = 7.41R_E$ .

To test the theory prediction for the growth rate, we use the band-pass filtered magnetic field data from  $\approx 13:28$ – $14:01$  UTC, as

**TABLE I.** Plasma parameters.

$A_{H^+} \equiv P_{\perp}/P_{\parallel} = 1.24,$	$\beta_{\parallel} = \beta_{\perp}/A_{H^+} = 3.90,$	$\beta_{\perp} = 4.84.$
$P_{\perp} = 10.7 \text{ nPa},$	$P_{\parallel} = P_{\perp}/1.24 = 8.62 \text{ nPa},$	$P_B = 2.21 \text{ nPa}.$
$n = 2.96 \text{ cm}^{-3},$	$v_{th\parallel} = 1.31 \times 10^6 \text{ m/s},$	$v_{th\perp} = 1.46 \times 10^6 \text{ m/s}.$
$\omega = 0.04 \text{ rad} \cdot \text{s}^{-1},$	$\Omega_{H^+} = 7.23 \text{ rad} \cdot \text{s}^{-1},$	$r_{gH^+}/R_E = 0.032.$
$\Gamma = 0.16,$	$k_{\perp} = 8.08 \times 10^{-7} \text{ rad} \cdot \text{m}^{-1},$	$k_{\parallel}/k_{\perp} = 0.16.$

shown in the inset in Fig. 8 (note that  $x \approx 500$ , so  $t = 500 \times 4 \text{ s} \approx 33 \text{ min}$ ). We assume a function of the form  $f(x) = \exp(\hat{\gamma}x) \sin(ax + c)$  and fit to the data using the Least Absolute Residual (LAR) robust nonlinear squares method (the LAR method minimizes the absolute distance of the residuals rather than the square of the residuals). With this method, we obtain  $\hat{\gamma} \approx 0.005$ ,  $a \approx 0.163$ ,  $c \approx -4.68$ , or  $\gamma = 0.005/4 = 0.00125 \text{ s}^{-1}$  and  $T = 4 \times 2\pi/(0.163) = 154.18 \text{ s}$ . The goodness of fit gives an r-square of 0.79 meaning that the parameters ( $\gamma$ ,  $T$ ,  $c$ ) obtained can explain about 79% of the variance in the measured wave data (excluding the outliers, here identified as higher frequency components), as shown in Fig. 8. The measurements agree very well with the theory prediction and vice versa. For completeness, the fitting results (with 95% confidence bounds) with the outliers included are  $\hat{\gamma} = 4.9 \times 10^{-3}$  ( $4.7, 5.0$ )  $\times 10^{-3}$ , and  $a = 0.162$  (0.161, 0.163) and  $c = -4.49$  ( $-4.74, -4.25$ ), with r-square 0.68.

Equation (1) assumes a Maxwellian distribution. In Fig. 9, we plot the energy spectrum for the H ion omni-fluxes  $j(E)$  at the time when the instability condition is satisfied. The spectrum follows rather well a Maxwellian distribution. The flux data (black) points were fitted (with a nonlinear least squares method) to the following Maxwellian formula for the fluxes:

$$j(E; T, A) = A \frac{E}{(k_B T)^{3/2}} \exp(-E/k_B T). \quad (3)$$

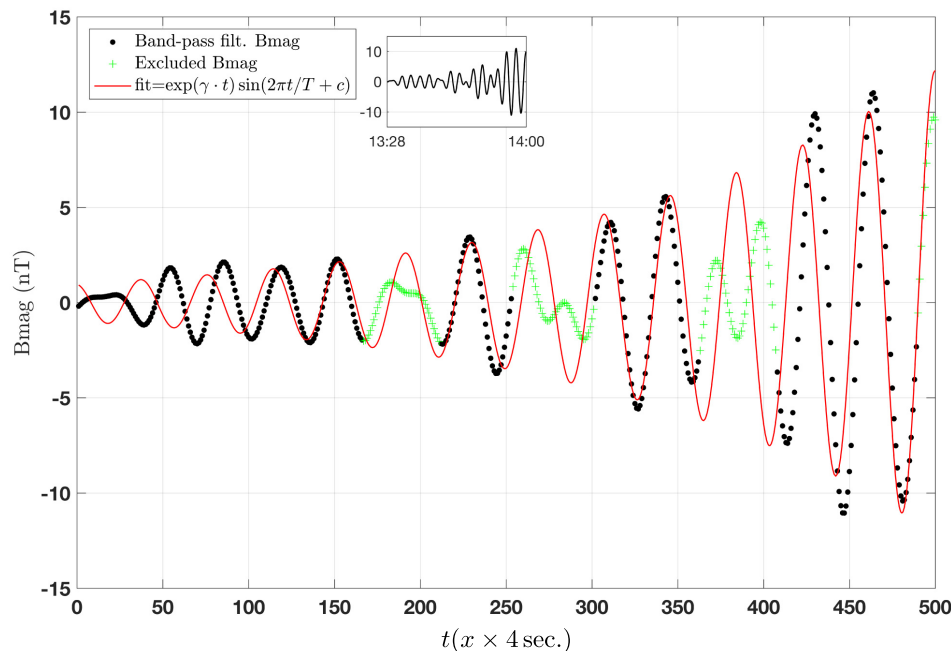


**FIG. 8.** Top inset: The band-pass filtered (3 dB at 4 mHz and 10 mHz cutoff frequencies) total magnetic field (from  $\approx 13:28$ – $14:01$  UTC). Magnified magnetic field data (black dots), same as the inset, obtained by the 4 s. resolution EMFISIS-B instrument. The red line is the fitted function (see the text) and the green crosses represent the outliers. The x-label represents the time elapsed since  $\approx 13:28$  UTC.

We obtain the following parameters  $k_B T = 19 \pm 3.1 \text{ keV}$ ,  $A = (1.78 \pm 0.19) \times (n/\sqrt{2m_H\pi^3}) = 3.7 \times 10^8 [\text{counts} \cdot \text{s}^{-1} \cdot \text{cm}^{-2} \cdot \text{MeV}^{-1}]$ .

According to theory,<sup>1</sup> the real frequency of the wave,  $\omega$ , is equal to the plasma diamagnetic drift frequency  $\omega_*$  which is given by

$$\omega = \omega_* \equiv \kappa \frac{k_{\perp} v_{th\parallel}^2}{\Omega}, \quad (4)$$

where  $\kappa \equiv d \ln n / dx$  is a measure of the density inhomogeneity in the perpendicular direction (with respect to the local magnetic field). From the measurements, we know all quantities in the equation for the frequency except  $\kappa$ ; therefore, we can estimate what the scale length of the inhomogeneity is, with the parameters shown in Table I, we obtain  $\kappa = 1.93 \times 10^{-7} \text{ m}^{-1} \approx 6.8/r$  ( $r = 5.6R_E$ ), which gives an inhomogeneity length of  $l_{\perp} = \kappa^{-1} = 0.83R_E$ . Corroboration for this estimate would require, however, multipoint measurements. Nevertheless, the inhomogeneity length obtained is slightly less than the typically assumed  $l_{\perp} \sim 1.86R_E$ , i.e.,  $\kappa = 3/r$  in other studies.<sup>1</sup>

## V. DISCUSSION

Data and theory show that DM mode instability is responsible for the event detected by Van Allen Probe B. In addition to the plasma instability being satisfied, there is good agreement between the predicted wave growth rate and the calculated rate from the measurements.

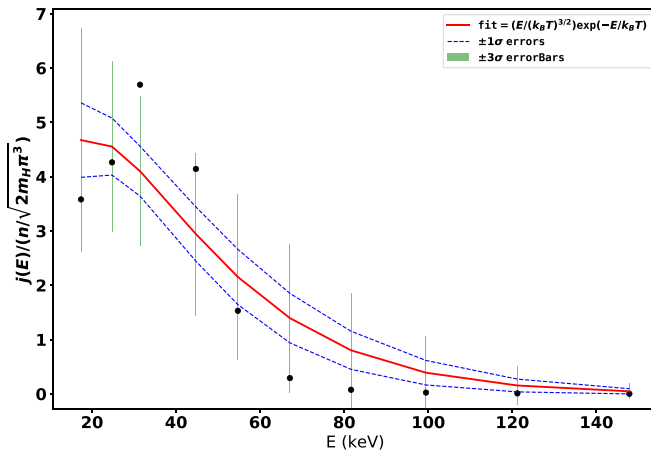


**FIG. 9.** Normalized H ion omni-fluxes (solid dots) vs Energy. Here,  $n/\sqrt{2m_H\pi^3} = 3.7 \times 10^3$  (counts  $\cdot$  s $^{-1}$   $\cdot$  cm $^{-2}$   $\cdot$  MeV $^{-1}$ ). The partial plasma density  $n = 4\pi \int_{E_{\text{min}}}^{E_j} dE \sqrt{m/2E} j(E) \approx 4\pi \sum_E \Delta E \sqrt{m/2E} j(E) = 2.96$  cm $^{-3}$ .

Our measurements and calculations herein used are based on the theoretical results predicted by the DM theory using the WKB approximation method in the perpendicular direction, and the *local* theory instability along the parallel direction.<sup>3</sup> So, it is necessary to provide some justification for this. First, the WKB approximation is valid when

$$\frac{1}{k_{\perp}} \left| \frac{dk_{\perp}}{dx_{\perp}} \right| \ll k_{\perp} \Rightarrow \frac{1}{l_{\perp}} \frac{\lambda_{\perp}}{2\pi} \ll 1. \quad (5)$$

From our estimations above, we have  $\lambda_{\perp} = 1.22R_E$  and  $l_{\perp} = 0.83R_E$ , so  $\lambda_{\perp}/(2\pi l_{\perp}) = 0.2$ . Hence, the WKB approximation is justified. Second, the instability condition Eq. (1), which here we rewrite as  $\Gamma > 0$  [recall,  $\Gamma = \beta_{\perp}(P_{\perp}/P_{\parallel} - 1) - 1$ ], is only valid locally. In general, however, the instability condition is a function of the position along the magnetic field line, which according to non-local theory<sup>3</sup> is  $\tau = 1 + (1/B)\partial P_{\perp}/\partial B < 0$ , where  $P_{\perp} = P_{\perp}(\psi, B)$  ( $\psi$  is the magnetic flux function). Note that in our notation  $\Gamma = -\tau_{\text{local}}$ . Thus, the magnetically trapped particles should be considered for the non-local DM instability, which becomes<sup>3</sup>  $(\tau \|B_{\parallel}\|^2) < 0$ ; here,  $(\dots) = (2/t_b) \int_{-s_m}^{s_m} (\dots) ds/v_{\parallel}$  represents the bounce averaging with magnetic turning points  $\pm s_m$ . Nevertheless, local theory is valid when<sup>3</sup> the mode width  $\Delta_k$  is

$$\Delta_k \sim 1/k_{\parallel} \ll d_{sm}, \quad (6)$$

i.e., less than the distance between two mirror points,  $d_{sm}$ . We note that  $d_{sm}$  is half the distance that a typical particle travels in a full bounce period, i.e.,  $d_{sm} = v_{\parallel} t_b/2$ . The reason is that  $t_b$ , see the above expression for the bounce averaging, is defined as the time it takes for a typical particle to travel back and forth between mirror points. Therefore, using<sup>31</sup>  $t_b = 43.1L/\sqrt{E}$ , we obtain  $d_{sm} = 5.65R_E$ , whereas  $\Delta_k = 1/k_{\parallel} = 7.41R_E/2\pi = 1.18R_E$ . Hence, the local instability analysis is also justified.

The partial plasma pressures for the six energy channels (above indicated) are numerically calculated as follows:

$$P_{\perp} = \pi \sum_{\alpha} \sum_E \sqrt{2m_H E} j(t_0, E, \alpha) \sin^3 \alpha \Delta E \Delta \alpha, \quad (7)$$

$$P_{\parallel} = 2\pi \sum_{\alpha} \sum_E \sqrt{2m_H E} j(t_0, E, \alpha) \sin \alpha \cos^2 \alpha \Delta E \Delta \alpha, \quad (8)$$

where the first sum in  $\alpha$  is over all pitch angles ( $0^{\circ}$ – $180^{\circ}$ ),  $t_0 \approx 13.28$  UTC,  $m_H = 938.3$  MeV/ $c^2$  is the proton rest mass, and  $c$  is the speed of light. (Note that all energies used are much less than the proton rest mass; therefore, the equations and formulae used are non-relativistic.) The sum in  $E$  is over the energy channels for  $E > 67.1$  keV. However, we should like to note that the fluxes for  $E > 67.1$  keV are so low compared to the first six energy channels ( $\approx 17$ – $67$  keV) that they do not contribute significantly to the pressures.

Note that we have provided error bars for the fitting formulae and other calculations except for the pressures. The reason is twofold. First, we expect the errors on the pressures to be extremely small. This is because of the high counts in the fluxes, due to the Poisson statistics, which go into the calculations for the pressures. Second, the RBSPICE level 3 PAP data used do not currently provide errors for the calculated moments (pressures and density). The file includes errors for each flux observation for all pitch angles and energies so we know that the Poisson statistical error for the  $90^{\circ}$  PA flux averaged over the time interval 13:20–14:40 is  $\sim 4\%$ . Therefore, we expect that these statistical errors will not have any significant impact on our main results/conclusions. Note as well that the partial pressures calculated here are based on the hot ion component of the plasma which is justified because the plasma pressure is dominated by the hot ion component; an estimate shows that the density of the hot plasma over that of the cold plasma is  $n_h/n_c \lesssim 10^{-1}$  and their respective temperatures are  $T_h \sim 10$ – $100$  keV and  $T_c \sim 10$ – $10^2$  eV, and thus,  $P_c/P_h \lesssim 10^{-2}$ . This is also consistent with the theoretical formulations for the DM instability, where it is assumed that the magnetospheric plasma consists of a cold core ion component and an energetic hot ion component, where the above ordering is needed to simplify the Vlasov-Maxwell system of equations.<sup>1,3</sup>

It is also important to note that the growth rate, Eq. (2), is valid for both mirror and drift-mirror modes. This is because, as explained in the introduction, the imaginary part of the dispersion relation (from which both the instability threshold and growth rate are obtained) is the same for both modes, see Hasegawa<sup>1</sup> Eqs. (23), (24), and (34).

As mentioned above, past measurements have failed to satisfy the instability condition Eq. (1). Therefore, much of the theoretical extensions to the theory (see, e.g., Refs. 19 and 20) have been put forward to lower the instability condition by including additional effects such as field line curvature effects and mode couplings (though the original theory of Hasegawa<sup>1</sup> did include inhomogeneity effects in density and magnetic field). The theory extensions are motivated by the fact that the DM instability threshold is difficult to satisfy in the inner magnetosphere, and other theoretical<sup>21</sup> and simulations<sup>22</sup> studies have concentrated on Finite Larmor Radius (FLR) effects for which  $k_{\perp} r_g \sim O(1)$ . They have shown that Drift Compressional Modes (DCM) can become unstable, for example, when the density gradient and proton temperature gradient are in opposite directions, i.e., without temperature anisotropy. However, for the event herein studied, the DM instability threshold is satisfied and we have that FLR effects are negligible ( $k_{\perp} r_g \ll 1$ ).

Therefore, we stress that this study has been able to corroborate the DM instability condition in its simplest form, thereby demonstrating that the DM theory developed by Hasegawa<sup>1</sup> captures most of the physics for this particular event.

Note that the calculated perpendicular wavelength is consistent with observations of compressional Pc 5 waves observed in the inner magnetosphere.<sup>36</sup> The great advantage of being able to measure and

corroborate the growth rate is that one can directly use the theory prediction to estimate the mode wavelength, whereas without the growth rate multipoint measurements or other techniques are needed.<sup>33</sup> We also checked for the contribution from the heavy ions, i.e., He and O ions. However, their fluxes are so low in this orbit that their pressure content is negligible for this particular event (see Cohen *et al.*,<sup>29</sup> Figs. 9 and 10).

## VI. CONCLUSIONS

1. We have presented evidence that the DM mode instability was responsible for generating the ultra-low frequency wave event on July 6, 2013 observed by Van Allen Probe B.
2. The DM plasma instability theory correctly explains the observed event. We found that the DM mode instability condition for bi-Maxwellian H ions is satisfied. The predicted maximum wave growth rate is  $0.0018 \text{ s}^{-1}$ . The observed growth rate is  $\approx 0.0013 \text{ s}^{-1}$ .
3. The estimated values for the perpendicular and parallel wavelengths are consistent with previous observations of internally generated ULF waves. The estimated inhomogeneity parameter (based on the wave frequency measured) is also within range of the typical values assumed in previous studies.
4. The data indicate that the energetic particle distribution from the combined energy channels is well represented by a Maxwellian distribution.
5. This study definitively shows that the ion anisotropy and pressure in the inner magnetosphere can be enough to generate large amplitude low frequency waves locally, otherwise thought to be generated by more extreme global events such as global magnetosphere compression, Kelvin-Helmholtz instability by the flow of solar wind around the magnetopause, etc.
6. Heavy ions appear in such sparse amount that they do not have an important effect on the DM mode instability for this event.

## ACKNOWLEDGMENTS

The work reported herein was supported by the NASA Van Allen Probes RBSPICE instrument project by JHU/APL subcontract 937836 to the New Jersey Institute of Technology under NASA Prime Contract No. NAS5-01072. L.C. and Z.X. acknowledge the support of the AFOSR grant of FA9550-16-1-0344 and NASA NNX15AF55G. A. R. Soto-Chavez would also like to acknowledge the support of the NSF Grant No. 1502923. The EMFISIS data were processed as work supported by JHU/APL 921647 under NASA Prime contract NAS5-01072. We also would like to thank discussions with Dr. Ilya Kuzichev and the larger RBSPICE and Van Allen Probes community. RBSPICE data are available at <http://rbspice.ftccs.com/Data.html>. EMFISIS data are available at <http://emfisis.physics.uiowa.edu/data/index>.

## REFERENCES

- <sup>1</sup>A. Hasegawa, *Phys. Fluids* **12**, 2642 (1969).
- <sup>2</sup>K. Miyamoto, *Plasma Physics and Controlled Nuclear Fusion*, Atomic, optical, and plasma physics (Springer, 2005), p. 62.
- <sup>3</sup>L. Chen and A. Hasegawa, *J. Geophys. Res.* **96**, 1503, <https://doi.org/10.1029/90JA02346> (1991).
- <sup>4</sup>D. J. Southwood and M. G. Kivelson, *J. Geophys. Res.* **98**, 9181, <https://doi.org/10.1029/92JA02837> (1993).
- <sup>5</sup>P. Porazik and J. R. Johnson, *J. Geophys. Res.* **118**, 7211–7218, <https://doi.org/10.1002/2013JA019308> (2013).
- <sup>6</sup>K. Takahashi, *Adv. Space Res.* **17**(10), 63 (1996).
- <sup>7</sup>L. J. Lanzerotti, C. G. MacLennan, and A. C. Fraser-Smith, *Geophys. Res. Lett.* **17**, 01593, <https://doi.org/10.1029/GL017i010p01593> (1990).
- <sup>8</sup>L. J. Lanzerotti and D. J. Southwood, *Hydromagnetic Waves, in Solar System Plasma Physics* (North-Holland, Amsterdam, 1979), pp. 109–135.
- <sup>9</sup>X. Li, M. Hudson, A. Chan, and I. Roth, *J. Geophys. Res.* **98**, 215, <https://doi.org/10.1029/92JA01540> (1993).
- <sup>10</sup>S. P. Gary, S. A. Fuselier, and B. J. Anderson, *J. Geophys. Res.* **98**, 1481, <https://doi.org/10.1029/92JA01844> (1993).
- <sup>11</sup>B. T. Tsurutani, E. J. Smith, R. R. Anderson, K. W. Ogilvie, J. D. Scudder, D. N. Baker, and S. J. Bame, *J. Geophys. Res.* **87**, 6060, <https://doi.org/10.1029/JA087iA08p06060> (1982).
- <sup>12</sup>C. Lacombe and G. Belmont, *Adv. Space Res.* **15**(8/9), 329 (1995).
- <sup>13</sup>C. Lacombe, F. G. E. Pantellini, D. Hubert, C. C. Harvey, A. Mangeney, G. Belmont, and C. T. Russell, *Ann. Geophys.* **10**, 772 (1992).
- <sup>14</sup>G. Haerendel, W. Baumjohann, E. Georgescu *et al.*, *Ann. Geophys.* **17**, 1592 (1999).
- <sup>15</sup>A. Vaivads, W. Baumjohann, G. Haerendel, R. Nakamura, H. Kucharek, B. Klecker, M. R. Lessard, L. M. Kistler, T. Mukai, A. Nishida, and C. T. Russell, *Ann. Geophys.* **19**, 311 (2001).
- <sup>16</sup>I. J. Rae, I. R. Mann, C. E. J. Watt, L. M. Kistler, and W. Baumjohann, *J. Geophys. Res.* **112**, A11203 (2007).
- <sup>17</sup>X. Zhu and M. Kivelson, *J. Geophys. Res.* **99**, 241, <https://doi.org/10.1029/93JA02106> (1994).
- <sup>18</sup>L. J. Lanzerotti, A. Hasegawa, and C. G. MacLennan, *J. Geophys. Res.* **74**, 5565, <https://doi.org/10.1029/JA074i024p05565> (1969).
- <sup>19</sup>O. A. Pokhotelov, V. A. Pilipenko, Y. M. Nezlina, J. Woch, G. Kremser, A. Korth, and E. Amata, *Planet. Space Sci.* **34**, 695 (1986).
- <sup>20</sup>J. Woch, G. Kremser, A. Korth, O. A. Pokhotelov, V. A. Pilipenko, Y. M. Nezlina, and E. Amata, *Planet. Space Sci.* **36**, 383 (1988).
- <sup>21</sup>C. Crabtree and L. Chen, *Geophys. Res. Lett.* **31**, L17804, <https://doi.org/10.1029/2004GL020660> (2004).
- <sup>22</sup>P. Porazik and Z. Lin, *Phys. Plasmas* **18**, 072107 (2011).
- <sup>23</sup>Z. Xia, L. Chen, L. Dai, S. G. Claudepierre, A. A. Chan, A. R. Soto-Chavez, and G. D. Reeves, *Geophys. Res. Lett.* **43**, 9444–9452, <https://doi.org/10.1002/2016GL070280> (2016).
- <sup>24</sup>A. R. Soto-Chavez, G. Wang, A. Bhattacharjee, G. Y. Fu, and H. M. Smith, *Geophys. Res. Lett.* **41**, 1838–1845, <https://doi.org/10.1002/2014GL059320> (2014).
- <sup>25</sup>B. H. Mauk, N. J. Fox, S. G. Kanekal, R. L. Kessel, D. G. Sibeck, and A. Ukhorskiy, *Space Sci. Rev.* **179**, 3–27 (2013).
- <sup>26</sup>D. Mitchell, L. Lanzerotti, C. Kim, M. Stokes, G. Ho, S. Cooper, A. Ukhorskiy, J. Manweiler, S. Jaskulek, D. Haggerty, P. Brandt, M. Sitnov, K. Keika, J. Hayes, L. Brown, R. Gurnee, J. Hutcheson, K. Nelson, N. Paschalidis, E. Rossano, and S. Kerem, *Space Sci. Rev.* **179**, 263 (2013).
- <sup>27</sup>A. R. Soto-Chavez, L. J. Lanzerotti, A. Gerrard, H. Kim, J. Bortnik, and J. W. Manweiler, *J. Geophys. Res. Space Phys.* **121**, 9547–9559, <https://doi.org/10.1002/2016JA022512> (2016).
- <sup>28</sup>C. Kletzing, W. Kurth, M. Acuna, R. MacDowall, R. Torbert, T. Averkamp, D. Bodet, S. Bounds, M. Chutter, J. Connerney, D. Crawford, J. Dolan, R. Dvorsky, G. Hospodarsky, J. Howard, V. Jordanova, R. Johnson, D. Kirchner, B. Mokrzycki, G. Needell, J. Odom, D. Mark, R. Pfaff, Jr., J. Phillips, C. Piker, S. Remington, D. Rowland, O. Santolik, R. Schnurr, D. Sheppard, C. Smith, R. Thorne, and J. Tyler, *Space Sci. Rev.* **179**, 127 (2013).
- <sup>29</sup>R. Cohen, A. J. Gerrard, L. J. Lanzerotti, A. R. Soto-Chavez, H. Kim, and J. W. Manweiler, *J. Geophys. Res. Space Phys.* **122**, 711–726, <https://doi.org/10.1002/2016JA022513> (2017).
- <sup>30</sup>W. Baumjohann and R. A. Treumann, *Basic Space Plasma Physics*, Revised ed. (Imperial College Press, 2012), pp. 30–33 and 50.
- <sup>31</sup>L. R. Lyons and D. J. Williams, *Quantitative Aspects of Magnetospheric Physics, Geophysics and Astrophysics Monographs* (Springer, 1984), pp. 24–26.
- <sup>32</sup>S. G. Claudepierre, I. R. Mann, K. Takahashi, J. F. Fennell, M. K. Hudson, J. B. Blake, J. L. Roeder, J. H. Clemmons, H. E. Spence, G. D. Reeves, D. N. Baker, H. O. Funsten, R. H. W. Friedel, M. G. Henderson, C. A. Kletzing, W. S. Kurth, R. J. MacDowall, C. W. Smith, and J. R. Wygant, *Geophys. Res. Lett.* **40**, 4491, <https://doi.org/10.1002/grl.50901> (2013).
- <sup>33</sup>K. Min, K. Takahashi, A. Y. Ukhorskiy, J. W. Manweiler, H. E. Spence, H. J. Singer, S. G. Claudepierre, B. A. Larsen, A. R. Soto-Chavez, and R. J. Cohen, *J. Geophys. Res. Space Phys.* **122**, 3013, <https://doi.org/10.1002/2016JA023770> (2017).
- <sup>34</sup>A. Grinstead, J. C. Moore, and S. Jevrejeva, *Nonlinear Process. Geophys.* **11**, 561 (2004); C. Torrence and G. P. Compo, *Bull. Am. Meteorol. Soc.* **79**, 61 (1998).
- <sup>35</sup>P. Hellinger, *Phys. Plasmas* **14**, 082105 (2007).
- <sup>36</sup>K. Takahashi, P. R. Higbie, and D. N. Baker, *J. Geophys. Res.* **90**, 1473, <https://doi.org/10.1029/JA090iA02p01473> (1985).